Journal of Computational Physics **183,** 623–651 (2002)
doi:10.1006/jcph.2002.7205

The Computational Modelling of Branching Fine Structures in Constrained Crystals[1]

Petr Klouček and Luis A. Melara

Department of Computational and Applied Mathematics, Rice University, 6100 Main Street, Houston, Texas 77005
E-mail: kloucek@rice.edu, luism@caam.rice.edu

Received December 10, 2001; revised September 13, 2002

We introduce a finite element method which is piecewise continuous on the microscopic scale of the spatial resolution h but discontinuous on the mesoscopic scale h^δ, $\delta \in (0, 1)$. The method is designed to capture the morphology of needle twin structures frequently found in ferric and pseudo-elastic crystals, namely, in uniaxial ferromagnets and au milieu of the Austenite-Martensite interfaces. The approach is based on a domain decomposition method that interpolates between the scale on order of the size of crystal and the microscopic scale of finite element approximation h. The scale interpolation is enabled by incorporating frequency adaptivity. The visualization and analysis of the computational results presented disclose microstructures corresponding to complex scaling laws. We document that the fine structures obtained by the presented method are not visible using classical formulation of the underlying variational problem and using conforming approximation of admissible sets. The proposed method is suitable for non-smooth relaxation and optimization when the minimizers lack the often required $C^{1,\alpha}$-regularity and when they exhibit fractal behavior.

1. INTRODUCTION

Our goal in this article is to develop a computational methodology for finding minimizers of the energies representing the work needed to create internal surfaces in constrained crystals. Our effort is motivated by the computational observations that classical tools

[1] The first author was supported in part by Grant NSF DMS-0107539. The work was supported by the Los Alamos National Laboratory Computer Science Institute (LACSI) through LANL Contract 03891-99-23, as part of the prime Contract W-7405-ENG-36 between the Department of Energy and the Regents of the University of California, by Grant NASA SECTP NAG5-8136, by a grant from Schlumberger Foundation, and by a grant from the TRW Foundation. The computations in this paper were performed on a 16 processor SGI Origin 2000, which was partly funded by NSF SCREMS Grant DMS-9872009.

0021-9991/02 $35.00

produce incorrect results in this framework. A simple mathematical model representing the energy of an internal surface reads

$$\min\{\mathcal{I}(u, \Omega) \mid u \in W^{1,4}(\Omega),\ u(x) = 0 \text{ on } \partial\Omega \text{ in the sense of traces}\}, \tag{1.1}$$

where $\Omega = (0, L) \times (0, K)$, $K > 0$, $L > 0$, and[2]

$$\mathcal{I}(u, \Omega) \stackrel{\text{def}}{=} \int_\Omega \alpha\, |\partial_x u(x, y)|^2\, dx\, dy + \int_\Omega \beta |(\partial_y u(x, y))^2 - 1|^2\, dx\, dy + \int_0^L \epsilon \|\partial_{yy} u(x, .)\|(0, K)\, dx. \tag{1.2}$$

The functional $\mathcal{I}(u, \Omega)$ has number of local minima at which the equilibrium metastable structures differ profoundly by pattern morphology. The lower the value of the minimum in (1.1), the more competing scales participate in the complexity of the structure of the minimizer. The global scaling properties of $\mathcal{I}$ associated with various types of local minimizers are studied analytically in [15–17]; the local scaling properties are derived in [6]. More recently, the problem is studied in [7], with $\beta = 1/\epsilon$, in order to derive a Γ-convergence result recovering an effective energy near internal domain walls in single crystals. Minimization of singularly perturbed non-convex functionals has a long history of intensive mathematical research. We refer the interested reader to these papers for a more comprehensive list of references and some historical background. Local minimizers of this class of problems pertain to the solid–solid and fluid–fluid phase transitions, as well as minimal surfaces.

The minimizers providing low values of the energy contained in the internal surfaces are difficult to obtain. Most constructions of such minimizers all have in common asymptotic self-similarity of the construction [2, 6,17]. The structures which develop in the "far-field" are scaled and redistributed with increasing frequencies close to the internal domain walls. From the computational point of view, the major problems are presented by the self-similarity leading to a fractal scaling and by the presence of the singular perturbation term $\int_0^L \epsilon \|\partial_{yy} u(x, .)\|(0, K)\, dx$. Within the classical finite element method, a conforming approximation would have to adhere to the $W^{2,\infty}$-topology. This is computationally expensive and it interferes with the local scaling properties of the approximate minimizers u_h due to their excessive smoothness. In these strong topologies, the approximation must be constructed using high-degree polynomials. The approximation in the weaker $W^{1,4}$-topology leads to the interpretation of the perturbation term as a Radon measure. There does not exist a direct, explicit way of implementing this term numerically in the weaker topology where the functional representing the arrangement work but excluding the so-called surface energy term is naturally defined.

The purpose of the paper is to reformulate for the computational purposes the original minimization problem (1.1) by removing the singular perturbation term and to replace its role by a *frequency equidistribution principle* in conjunction with a priori imposed global scaling laws. Our approach can be applied in situations which are mathematically similar such as minimization of the non-local functional in (2.5). We apply the proposed

[2] The different powers of the partial derivatives put more emphasis on the distance of $\partial_x u$ from zero if $\beta < 1$. We could certainly choose an anisotropic space for the admissible functions. The choice of the Sobolev space $W^{1,4}(\Omega)$ is more a choice of convenience.

methodology to obtain computationally complex multiscale minimizers corresponding to the equilibria of the total stored energy of domain walls in pseudo-elastic and ferro-elastic materials which includes the sharp interface approximation of the twin boundaries. We are not aware of any numerical or computational method providing finite element approximation of the self-similar minimizing patterns. One of our goals is to address this gap. We also provide analysis of the computational results studying various scaling laws including those which are conjectured but not proven at a time in the available literature.[3]

The computational recovery of complex multiscale minimizers of functionals similar to (1.2) is important. The numerics is much less dependent on a particular form of the energy functional. This is certainly not true for analytical works. More importantly, as noted in [3, 4], most of the analytical methods use periodic or semi-periodic structures to estimate the effective energy. Such approach is certainly justified when the lower bound for the energy is available and if such structures attain the scaling predicted by the lower estimates. If this were not the case, then numerics has the potential to reveal perhaps non-periodic minimizing structures including their local scaling properties, which are not readily available using analytical tools. Another application of the numerical approach is to uncover a variety of fine structures or microstructures corresponding to predicted scaling laws. This detailed information is perhaps not important for the effective macroscopic behavior but plays a crucial role if other effects such as heat transfer or oscillating electric field are taken into account.

The paper is organized as follows. We describe global scaling laws and the corresponding fine structures in Section 2. We outline the mesoscale nonconforming method in Section 3. We present the reformulation of the minimization problem (1.1) in Section 4. The computational examples are described and various comparisons, including observed scaling laws, are provided in Section 5.

1.1. Internal Surfaces in Crystals

Internal surfaces in crystals form domain walls in many different classes of materials. Ferroelastic or pseudo-elastic materials represent certainly a valid example. These pattern boundaries are typically the result of a phase transition between two phases with different symmetries. The underlying phase transition thus often creates twin structures. Twins are seen to form when a crystal is squeezed or subjected to an external field. Mechanical twinning is technologically important in superconductors and industrial shape memory alloys, and it is observed in mineralogically and petrologically relevant systems. Major mesoscale microstructures formed by twins include junctions where twins intersect, S-shaped domain walls, and needle twins. In order to describe the geometrical and physical properties of such internal surfaces, the energy of the domain wall may be considered. This energy has the form [22]

$$\mathcal{J} = \int W(q)\, d\Omega + \Sigma \int (e_s)_i \sigma_i \, d\Omega + \int \sigma_{\mathrm{w}} \, dS. \tag{1.3}$$

The first contribution in (1.3) represents the Landau potential calculated by the spatial

[3] The numerical results presented confirm a local scaling properties of the multiscale minimizers conjectured in [17]. It has been pointed out to us by an unanimous referee that these conjectures were proved correct in [6] at about the same time that we have been investigating them computationally.

summation of the density W corresponding to an order parameter q on a mesoscopic scale for areas in the crystal that are close to an internal surface. The second contribution includes the interaction between the spontaneous strain and a stress field. The last term accounts for the surface energy.

From the mathematical point of view, a pattern morphology such as the needle twins corresponds to very low levels of energy $\mathcal{J}$. Various mesoscale microstructures are located at different local minima of $\mathcal{J}$. The numerical approach to finding these patterns by minimization of the energy $\mathcal{J}$ is rather difficult since commonly observed patterns in ferroelastic domains or twinned pseudo-elastic materials are formed by a competition of events occurring on many different scales.

2. GLOBAL SCALING AND THE UNDERLYING FINE STRUCTURES

We consider the following two examples to illustrate how the complexity of internal surfaces in crystals can grow as the energy decreases. In the framework of the ferric materials, the (micromagnetic) energy (1.3) of a domain wall in an uniaxial ferromagnet given by

$$\mathcal{J}(\mathbf{m}) \stackrel{\text{def}}{=} \alpha \int_{\mathbb{R}^2} |\nabla u(x)|^2 \, dx + \beta \int_{\Omega} m_2(x)^2 \, dx + \epsilon \int_{\Omega} |\nabla \mathbf{m}(x)| \, dx, \tag{2.1}$$

where $\mathbf{m} = (m_1, m_2)$, $|\mathbf{m}| = 1$, and $\Delta u = \operatorname{div} \mathbf{m}$ in Ω, $\mathbf{m} = 0$ in Ω^c, and $\Omega = (-L, L) \times (0, 1)$, is considered in [5]. The unknown $\mathbf{m}$ represents spontaneous magnetization. The first term represents the non-local magnetic field energy, the second term yields micromagnetic anisotropy, and the last term represents local surface energy associated with the presence of the Bloch walls which correspond to twins found in Martensitic materials. The energy (2.1) is derived in [5] as the sharp interface approximation from a more standard Landau–Lifshitz theory [18]. Investigating the local minimizers of (1.3), it is possible to describe the formation and geometrical structure of magnetic microdomains. The available results indicate that there are two different regimes of optimization at which a local minimum of the stored energy $\mathcal{J}(\mathbf{m})$ is attained, [5]. Namely, disregarding the anisotropy term,

$$\min \mathcal{J}(\mathbf{m}) \text{ scales as } \begin{cases} \alpha^{1/2} \epsilon^{1/2} L^{1/2}, & \text{for "one dimensional patterns",} \\ \alpha^{1/3} \epsilon^{2/3} L^{1/3}, & \text{for "multi-dimensional patterns" if } \frac{\epsilon}{L} \text{ is small.} \end{cases} \tag{2.2}$$

The first regime has been known for a long time [18]. It follows by simply investigating the energy $\mathcal{J}(\mathbf{m})$, Eq. (2.1), for the divergence-free magnetization $\mathbf{m} = (\pm 1, 0)$ that eliminates the crystalline anisotropy. The micromagnetic energy then behaves as [5, 18]

$$\mathcal{J}(\mathbf{m}) \propto \alpha a + \epsilon \frac{L}{a}, \tag{2.3}$$

where a is the layer width, and the surface energy is proportional to $\epsilon \frac{L}{a}$. The minimum with respect to a in (2.3) is attained for

$$a = \sqrt{\frac{\epsilon L}{\alpha}}, \quad \text{i.e., } \mathcal{J}_{\text{OPT}}(\mathbf{m}) \propto \alpha^{1/2} \epsilon^{1/2} L^{1/2}. \tag{2.4}$$

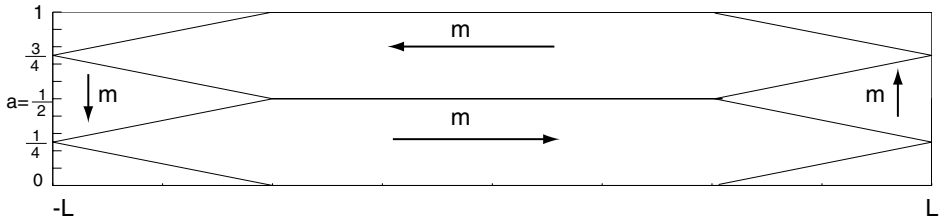

FIG. 1. The function plotted on this figure is an example of a minimizer corresponding to the first scaling law (2.2a). This shows the relationship between the surface energy and the elastic energy. The surface energy term is $\epsilon L/a$. We have $a = 1/2$. The surface energy plays role of the counter of the number of laminates along the y-direction.

Clearly, since $\mathbf{m} = 0$ in Ω^c the energy is not zero in the triangular regions close to $x = -L$ and $x = L$; cf. Fig. 1. As L increases, the excess energy contained in the triangular regions increases. Consequently, for L large enough the first regime is not optimal. Thus, there must exist a different pattern corresponding to a different local minimum of $\mathcal{J}(\mathbf{m})$ for the system to be stable. We note that if $\epsilon/L < \alpha$ then $\alpha^{1/2}\epsilon^{1/2}L^{1/2} > \alpha^{1/3}\epsilon^{2/3}L^{1/3}$. The second regime in (2.2) is thus preferable for "long" crystals.

The geometrical structures having the energy scaled as in the second regime in (2.2) are studied in a number of works. The first studies were done in the framework of the structure of the Austenite–Martensite Interface in [15–17], and then computationally including quasi-statics based on a level-set approach in [10, 12, 23]. Recently, the morphology of the second regime has been studied in the framework of micromagnetic in [5, 9], in the framework of diblock copolymers in [4], and using an abstract apparatus of probability measures on multiscale micropatterns in [1].

The lower bound for the energies like $\mathcal{J}(\mathbf{m})$ can be obtained using interpolation inequalities [4]. Restricting the discussion to one dimension, $\Omega = (0, L)$, the micromagnetic energy $\mathcal{J}(\mathbf{m})$ becomes similar to energies studied in [1, 15] and more recently in [19]. With the change $m = \dot{u}$, the energy may be considered in a less frequently used form [4, 19]

$$\mathcal{J}(u) \stackrel{\text{def}}{=} \alpha \|u\|^2_{H^{-1}(0,L)} + \int_0^L \beta W(\dot{u}(x)) + \epsilon^2 |\ddot{u}(x)|^2 \, dx, \tag{2.5}$$

where the density W is such that it forces $\dot{u}$ to be close to ± 1; e.g., $W(s) = (s^2 - 1)^2$. The energy (2.5) corresponds to the energy introduced in (2.1), except a different norm is used in place of the non-local term. The presence of $\epsilon^2 |\ddot{u}(x)|^2$ as opposed to $\epsilon |\ddot{u}(x)|$ corresponds to the Landau–Lifshitz representation of the surface energy [18]. The singular term in (2.1) represents a sharp interface approximation of the twin boundaries. The connections between the two models are discussed in detail in [15]. We refer to [4] for interpretation of the term $\alpha \|u\|^2_{H^{-1}(0,L)}$ as the *non-local energy*.

We re-derive a lower bound for the energy having the form (2.5). Let $v(s) = \sum_{k=-\infty}^{\infty} v_k \exp(2\pi i k s)$ be one-periodic function with a zero mean. Then

$$\|v\|^2_{H^{-1}(0,1)} = 2\pi \sum_{k=-\infty, k\neq 0}^{\infty} \frac{|v_k|^2}{k^2}.$$

Using the following inequality [4], with $\lambda > 0$, Λ integer, $v \in W^{1,2}(0, L)$, $|v| \leq 1$,

$$C\int_0^1 |v(x)|^2\,dx \leq \frac{1}{\Lambda}\left(\int_0^1 \frac{1}{\lambda}W(v) + \lambda\,|\dot{v}(x)|^2\,dx\right) + \sum_{k=-\infty,k\neq 0}^{\infty} \min\left\{1, \frac{\Lambda^2}{k^2}\right\}|v_k|^2 \quad (2.6)$$

we can establish a lower bound for the energy $\mathcal{J}(u)$ in (2.5). The change of variables $x = Ly$, $\delta > 0$, yields after some manipulations [13]

$$\begin{aligned}\mathcal{J}(u) &= \alpha\,\|u\|^2_{H^{-1}(0,L)} + L\int_0^L \frac{\beta}{L}W\left(\dot{u}(x)\right) + \left(\frac{\epsilon}{\sqrt{L}}\right)^2 |\ddot{u}(x)|^2\,dx \\ &= L^2\alpha\left(\frac{\epsilon}{L^{\frac{5}{2}}\alpha}\right)^{\delta} Y, \end{aligned} \quad (2.7)$$

where

$$\begin{aligned} Y = &\left(\frac{\epsilon}{L^{\frac{5}{2}}\alpha}\right)^{-\delta}\|u\|^2_{H^{-1}(0,1)} + \left(\frac{\epsilon}{L^{\frac{5}{2}}\alpha}\right)^{1-\delta}\int_0^1 \left(\frac{\epsilon}{L^{\frac{5}{2}}}\right)^{-1}\frac{\beta}{L}W\left(\frac{1}{L}\frac{d}{dy}u(Ly)\right) \\ &+ \frac{\epsilon}{L^{\frac{5}{2}}}\left|\frac{d^2}{dy^2}u(Ly)\right|^2 dy. \end{aligned}$$

We assume that

$$\frac{1}{L}W\left(\frac{s}{L}\right) \geq (s^2-1)^2, \quad \text{for } L > 1, \text{ and for } s \text{ close to } \pm 1.$$

Taking $\lambda = \epsilon/L^{\frac{5}{2}}$, $\delta = 2/3$, and $\Lambda = (\frac{\epsilon}{L^{\frac{5}{2}}\alpha})^{-1/3}$, we now have the possibility to apply the inequality (2.6), with v replaced by $\dot{u}$. If $\epsilon/L < \alpha$ then

$$2\pi\sum_{k=-\infty,k\neq 0}^{\infty}\min\left\{1, \frac{\Lambda^2}{k^2}\right\}|v_k|^2 = \Lambda^2\,\|v\|^2_{H^{-1}(0,1)}\,.$$

Consequently, the interpolation inequality (2.6) provides a positive constant C such that

$$C\int_0^1 |\dot{u}(x)|^2\,dx \leq Y. \quad (2.8)$$

Thus (2.8) and (2.7) yield

$$\mathcal{J}(u) \geq CL^2\alpha\left(\frac{\epsilon}{L^{\frac{5}{2}}\alpha}\right)^{2/3}\int_0^1 |\dot{u}(x)|^2\,dx. \quad (2.9)$$

Assuming $\int_0^1 |\dot{u}(x)|^2\,dx = 1$, we have

$$\mathcal{J}(u) \geq C\alpha^{1/3}\epsilon^{2/3}L^{1/3}. \quad (2.10)$$

We refer to [4, 5] for the upper bounds which are, up to a multiplicative constant, the same as the lower bound (2.10).

A construction of Privorotskij [20] provides a minimizer yielding the second global scaling; see, e.g., [5, 14]. The interpolation inequalities such as (2.6), namely the lower bounds they provide, indicate optimality of these constructions. See Fig. 2.

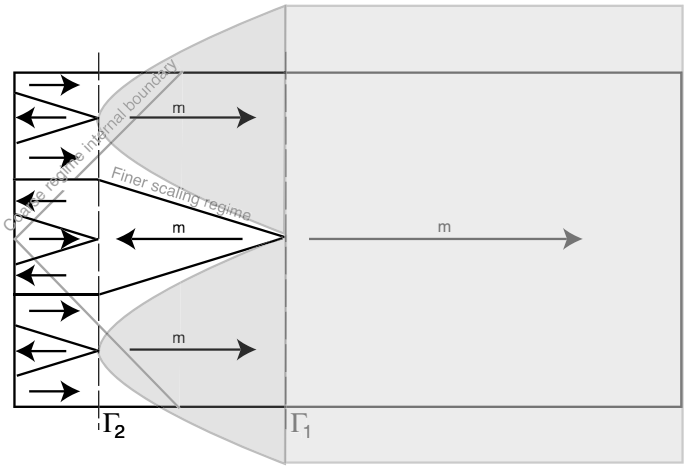

FIG. 2. Microscale construction covered by a mesoscale, optically visible, needle twin structure corresponding to the Privorotskij construction [20].

3. NONCONFORMING MESO-SCALE COMPUTATIONAL APPROACH

The standard approximation and optimization tools applied to the problem (1.1) do not capture the multidimensional patterns discussed in Section 2. We provide computational evidence of this deficiency by using a conforming approach to relax the functional $\mathcal{I}$ in Section 5. We strive to derive an optimization approach based on the minimization of the functional $\mathcal{I}(u, \Omega)$, (1.2), but we try to avoid the explicit inclusion of the singular perturbation (surface energy) term $\int_0^L \epsilon \|\partial_{yy} u(x, .)\|(0, K)\, dx$. This term represents the total variation of the second derivatives of the function u. The presence of the singular perturbation term in the definition of the function $\mathcal{I}(u, \Omega)$ guarantees existence of the strong limit of any minimizing sequence in, say, $W^{1,4}(\Omega)$. Consequently, it guarantees attainment of the minimization problem (1.1). We note that taking into account only the first two terms in (1.2) yields a minimization problem with non-attainable infimum for there is no mechanism imbedded into the structure of the functional to prevent creation of unlimited oscillations in the gradient of the minimizer.

We replace the singular term representing the surface energy by the *frequency equidistribution principle*. This approach consists in the decomposition of the domain Ω into infinite number of subdomains. We construct the minimizers in such a way that the number of discontinuities in their gradients is controlled by the measure of these subdomains to guarantee a strong convergence of minimizing sequences. We prove the following result to set a stage for the non-conforming approach.

THEOREM 3.1. *Let $\Omega = (0, L) \times (0, K)$, $L, K > 0$, and let $\{u_n\}_{n\in\mathbb{N}} \subset W^{1,p}(\Omega)$, $p > 2$, be a uniformly (w.r.t. n) bounded sequence. Let us denote its weak limit by $u \in W^{1,p}(\Omega)$. Let us assume that $u_n = 0$ on $\partial\Omega$ for any $n \in \mathbb{N}$, and let $\partial_y u_n(x, y) \in \{\pm 1\}$ for a. a. $x \in \Omega$. Then*

$$\int_0^K \int_0^L |\nabla u_n(x, y) - \nabla u(x, y)|^2 \, dx\, dy$$
$$\leq \mathcal{P}(n) + \|u_n - u\|_{L^\infty((0,L)\times(0,K))} \int_0^L \|\partial_{yy} u_n(x, .)\|(0, K)\, dx, \tag{3.1}$$

where

$$\mathcal{P}(n) \stackrel{def}{=} \|\partial_x u_n - \partial_x u\|^2_{L^2(\Omega)} + \int_0^K \int_0^L (\partial_y u_n(x, y) - \partial_y u(x, y))\partial_y u(x, y)\, dx\, dy.$$

Let us assume that

$$\|\partial_x u_n - \partial_x u\|_{L^2(\Omega)} \to 0 \quad \text{as } n \to \infty. \tag{3.2}$$

Then, in particular, u_n converges to its weak limit strongly in $W^{1,p}(\Omega)$ if

$$\begin{gathered}\lim_{n\to\infty} \|u_n - u\|_{L^\infty((0,L)\times(0,K))} \int_0^L \|\partial_{yy} u_n(x, .)\|(0, K)\, dx = 0, \quad \text{or} \\ \lim_{n\to\infty} \int_0^L \|\partial_{yy} u_n(x, .)\|(0, K)\, dx < +\infty.\end{gathered} \tag{3.3}$$

Remark 3.2. Here $\|\partial_{yy} u(x, .)\|(0, K)$ denotes the total variation of $\partial_{yy} u(x, .)$ at point x and with the second variable in $(0, K)$ (Definition 5.1.1 [24]). The second derivative of u becomes a Radon measure if $\partial_y u \in \{\pm 1\}$. The total variation can be identified in our situation with the essential variation $\operatorname{essV}_0^K(\partial_y u)$ given by (Exercise 5.1 [24])

$$\operatorname{essV}_0^K(\partial_y u) = \sup\left\{\sum_{k=1}^{l} |\partial_y u(x, y_k) - \partial_y u(x, y_{k-1})|\right\}, \tag{3.4}$$

where the supremum is taken over all finite partitions $0 < y_0 < y_1 < \cdots < y_l < K$ such that each point y_i is a point of approximate continuity with respect to Lebesgue measure.

Remark 3.3. We note that the second condition in (3.3) is not automatically satisfied. As an example we can consider unidirectional laminates which will have zero x-derivative but their y-derivative will uncontrollably oscillate between ± 1. The limiting microstructure will indeed satisfy the homogeneous boundary conditions but the number of jumps in the y-derivative will not be bounded.

Proof (of Theorem 3.1). We have

$$\begin{aligned}&\int_0^K \int_0^L |\nabla u_n(x, y) - \nabla u(x, y)|^2\, dx\, dy \\ &\quad = \mathcal{P}(n) + \int_0^K \int_0^L (\partial_y u_n(x, y) - \partial_y u(x, y))\partial_y u_n(x, y)\, dx\, dy \\ &\quad = \mathcal{P}(n) + \int_0^L \sum_{i=1}^{M(n)-1} \int_{y_i^n}^{y_{i+1}^n} (\partial_y u_n(x, y) - \partial_y u(x, y))\partial_y u_n(x, y)\, dx\, dy \\ &\quad = \mathcal{P}(n) + \int_0^L \sum_{i=1}^{M(n)-1} (u_n(x, y) - u(x, y))|_{y=y_i^n}^{y=y_{i+1}^n} \partial_y u_n\left(x, \psi_i^n\right) \\ &\quad = \mathcal{P}(n) + \int_0^L \sum_{i=1}^{M(n)-1} \left(u_n\left(x, y_i^n\right) - u\left(x, y_i^n\right)\right)\left[\partial_y u_n\left(x, y_i^n\right)\right].\end{aligned} \tag{3.5}$$

In deriving (3.5), we assume that $\{y_i^n\}_{i=1}^{M(n)}$ are the only points where $\partial_y u_n$ suffer a jump, and $\psi_i^n \in (y_i^n, y_{i+1}^n)$ is arbitrary. We denote by [.] the jump of the enclosed quantity. Since, in view of the definition (3.4)

$$\left| \int_0^L \sum_{i=1}^{M(n)-1} \big(u_n(x, y_i^n) - u(x, y_i^n)\big) \big[\partial_y u_n(x, y_i^n)\big] \right| \leq \|u_n - u\|_{L^\infty((0,L)\times(0,K))} \int_0^L \|\partial_{yy} u_n(x, .)\|(0, K)\, dx \tag{3.6}$$

(3.1) follows.

The strong convergence in $W^{1,2}(\Omega)$ follows from (3.1) since $\mathcal{P}(n) \to 0$ as $n \to \infty$. Indeed, the assumption (3.2), the continuous imbedding of $W^{1,p}(\Omega)$ into $C^{0,\lambda}(\Omega)$ for $p > 2$ which guarantees the strong convergence of the L^∞ norm, and from the assumed weak convergence of the sequence, we conclude that $\mathcal{P}(n) \to 0$ in view of either of the assumptions (3.6). ■

Remark 3.4. (i) We do not assume that $\partial_x u_n \to 0$ since the differential inclusion $\nabla u \in \{(0, \pm 1)\}$ subject to the pointwise Dirichlet boundary condition $u = 0$ on $\partial\Omega$ does not have a solution. On the other hand the inclusion $\nabla u \in \{(\pm\epsilon, \pm 1)\}$, $\epsilon > 0$, is solvable. This is because the homogeneous Dirichlet condition has its gradient contained in $\{\pm\epsilon, \pm 1\} \cup \text{Int Co}\{\pm\epsilon, \pm 1\}$ (Theorem 1.4 [8]). Here, Int Co denotes the interior of the convex hull of the set $\{\pm\epsilon, \pm 1\}$.

3.1. Implementation in a Finite Dimensional Setting

In a finite dimensional setting, we split the domain $(0, L) \times (0, K)$ into subdomains $(0, L_i) \times (0, K)$, $L_{i+1} < L_i$, $i = 1, 2, \ldots, M(h) - 1$. We have for $u_h \in V_h^{(i)}$

$$\sup_{x \in (L_{i+1}, L_i)} \|\partial_{yy} u_h(x, .)\|(0, K) \leq \frac{1}{\sqrt{2}} \dim V_h^{(i)} \tag{3.7}$$

where

$$V_h^{(i)} = \{v_h \in C^0(\Omega_i) | v_h|_{Q_h} \in Q_1\}, \tag{3.8}$$

$Q_h \in \tau_h^{(i)}$ is (for simplicity) a uniform partitioning of the subdomain Ω_i, i.e., $\Omega_i = (L_i - L_{i+1}) \times (0, K) = \bigcup_h Q_h$ and $Q_1 = \text{Span}\{1, x, y, xy\}$. Thus

$$\|\nabla u_h(x, y) - \nabla u(x, y)\|^2_{L^2((0,L)\times(0,K))} \leq \mathcal{P}(h) + \|u_h - u\|_{L^\infty((0,L)\times(0,K))} \sum_{i=1}^{M(h)-1} (L_i - L_{i+1}) \dim\big(V_h^{(i)}\big). \tag{3.9}$$

Hence, we can guarantee the strong convergence of the approximating sequence u_h in at least $W^{1,2}((0, L) \times (0, K))$, and by interpolating inequalities in $W^{1,\infty}$ if an uniform L^∞-bound

for gradients is available, by requiring

$$\begin{aligned} u_h &\rightharpoonup u \quad \text{weakly in } W^{1,p}((0,L)\times(0,K)), \quad p \geq 3, \\ \mathcal{P}(h) &\to 0 \quad \text{as } h \to +0, \\ &\lim_{M(h)\to+\infty} \sum_{i=1}^{M(h)-1} (L_i - L_{i+1}) \dim V_h^{(i)} < +\infty. \end{aligned} \tag{3.10}$$

3.2. Dimension of $V_h^{(i)}$

We seek a sequence of functions $u_h^{(i)} \in V_h^{(i)}$, $i = 1, 2, \ldots, M(h)$. Now we determine an appropriate dimension of the space $V_h^{(i)}$. It follows from the theory developed in [16] that there exists a constant C, independent of u, ϵ, and L, such that a multiscale minimizer obeys the inequality

$$\int_0^L \|\partial_{yy} u(x,.)\|(0,1)\,dx \leq C\epsilon^{-1/3} L^{1/3}. \tag{3.11}$$

We assume that the same inequality is true on the mesoscopic scale $L_i - L_{i+1}$. Consequently, we require

$$\dim V_h^{(i)} \leq \epsilon^{-1/3}(L_i - L_{i+1})^{-2/3} \tag{3.12}$$

to obtain the mesoscopic scaling

$$\int_{L_{i+1}}^{L_i} \|\partial_{yy} u(x,.)\|(0,1)\,dx \leq \dim V_h^{(i)}(L_i - L_{i+1}) \leq \epsilon^{-1/3}(L_i - L_{i+1})^{1/3}. \tag{3.13}$$

Thus we have for $u_h^{(i)} \in V_h^{(i)}$

$$\begin{aligned} \int_0^L \left\|\partial_{yy} u_h^{(i)}(x,.)\right\|(0,K)\,dx &= \sum_{i=1}^{M(h)} \int_{L_{i+1}}^{L_i} \left\|\partial_{yy} u^{(i)}(x,.)\right\|(0,K)\,dx \\ &\leq \epsilon^{-1/3} \sum_{i=1}^{M(h)} (L_i - L_{i+1})^{1/3} \\ &= \epsilon^{-1/3} L^{1/3} \sum_{i=1}^{M(h)} \left(\frac{L_i - L_{i+1}}{L}\right)^{1/3} \end{aligned} \tag{3.14}$$

We impose the following summability condition to comply with (3.10c):

$$\lim_{M(h)\to+\infty} \sum_{i=1}^{M(h)} \left(\frac{L_i - L_{i+1}}{L}\right)^{1/3} < +\infty. \tag{3.15}$$

We note that (3.15) and (3.12) yield (3.10c).

4. FORMULATION OF THE OPTIMIZATION PROBLEM

We consider the minimization of the functional (4.1) separately on each subdomain Ω_i. Consequently, we replace the minimization problem (1.1) with the following optimization

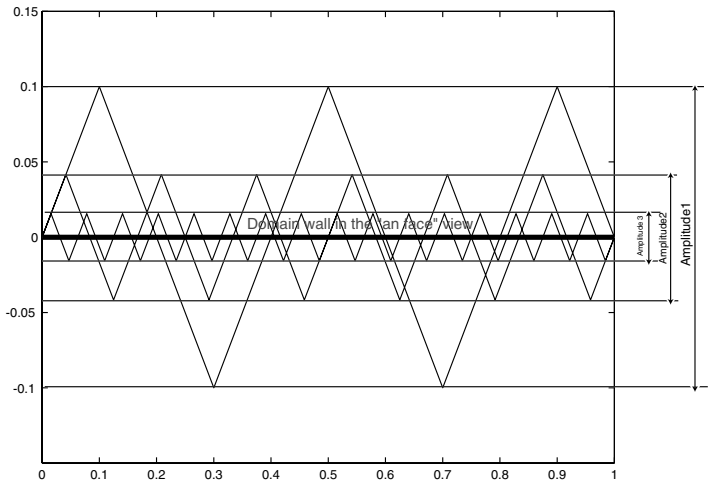

FIG. 3. A cross-sectional view of a typical behavior of the minimizers of (1.2) as they approach the boundary at $x = 0$. Since $\nabla u = (0, \pm 1)^T$ the function cannot meet the homogeneous boundary condition. This forces the function to oscillate faster and faster, simulated by amplitudes 1–3 on the picture, as it approaches the domain wall simulated by the "hard" boundary condition $u = 0$.

problem. Let us denote for simplicity the first two terms in (1.2) by $\mathcal{J}(u, \Omega)$, i.e.,

$$\mathcal{J}(u, \Omega) \stackrel{\text{def}}{=} \int_\Omega \alpha \, |\partial_x u(x, y)|^2 \, dx \, dy + \int_\Omega \beta |(\partial_y u(x, y))^2 - 1|^2 \, dx \, dy. \tag{4.1}$$

Problem 4.1. Let $\Omega = (0, L) \times (0, K), L > 0, K \geq 1$, and $\alpha > 0, \beta > 0, \gamma > 0, \epsilon > 0$ be given. Let the subdomains $\Omega_i = (L_{i+1}, L_i) \times (0, K)$ such that $L_{i+1} < L_i$, for any $i = 1, 2, \ldots, M-1$, $L_M = 0$, and $\Omega = \cup_{i=1}^M \Omega_i$ be given. Let us denote $\Gamma_{i+1} \stackrel{\text{def}}{=} \partial\Omega_{i+1} \cap \partial\Omega_i$. Let us assume that the partition points L_i satisfy the condition (3.15). We seek a vector $\{u^{(i)}\}_{i=1}^M$, $u^{(i)} \in W^{1,4}(\Omega_i)$, by solving

$$\begin{aligned}
&\min_{\substack{u^{(i)} \in W^{1,4}(\Omega_i) \\ i=1,2,\ldots,M}} \sum_{i=1}^{M} \mathcal{J}\big(u^{(i)}, \Omega_i\big) + \gamma \sum_{i=1}^{M-1} \int_{\Gamma_i} \int_{\Gamma_i} \big| w^{(i+1,i)}(x) - w^{(i+1,i)}(y) \big|^2 \, dx \, dy, \\
&\text{where } w^{(i+1,i)} = u^{(i+1)} - u^{(i)}, \quad \gamma > 0, \\
\text{subject to} \quad &\int_{L_i}^{L_{i+1}} \big\| \partial_{yy} u^{(i)}(x, .) \big\| \, (0, K) \, dx \leq C \epsilon^{-1/3} \, (L_i - L_{i+1})^{1/3} \, K, \\
&u^{(M)}(x, y) = 0, \qquad \text{on } \partial\Omega_M \backslash \{x = L_{M-1}\}, \\
&u^{(i)}(x, y) = 0, \qquad \text{on } \partial\Omega_i \backslash \{\{x = L_i\} \cup \{x = L_{i-1}\}\}, \\
&\nabla u^{(1)}(x, y) n = 0, \quad \text{on } \{x = L_1\}, \\
&\text{for any} \quad i = 1, 2, \ldots, M(h) - 1.
\end{aligned} \tag{4.2}$$

Remark 4.2. We do not require the continuity of the minimizers across the interfaces Γ_i, hence the attribute nonconforming.

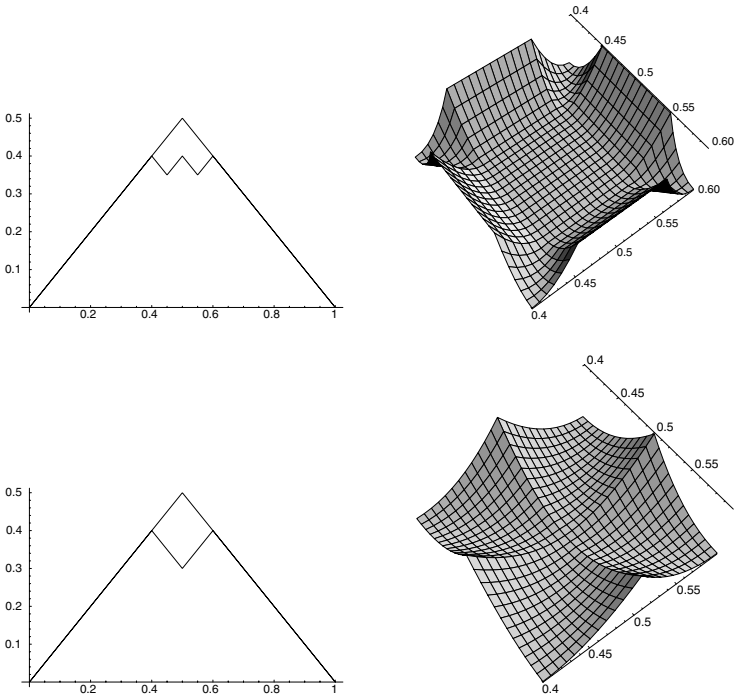

FIG. 4. The first plot, top-left, shows superposition of two function: function f which has derivatives $+1$ in $[0, 1/2)$ and -1 in $(1/2, 1]$ and the function g which has derivatives also ± 1, oscillating in the intervals (0, 0.4), (0.4, 0.45), (0.45, 0.5), (0.5, 0.55), (0.55, 0.6), (0.6, 1.0). Its "coupling energy," measured by the term $\sqrt{\int_{\Gamma_i}\int_{\Gamma_i} |w_h^{(i+1,i)}(x) - w_h^{(i+1,i)}(y)|^2\,dx\,dy}$, is 0.047. The picture on the top-right shows $(f(x) - g(x) - (f(y) - g(y)))^2$ close to the center of the square $(0, 1)^2$. The lower two pictures show the similar computations but for different functions f and g. The "coupling energy" of the lower case is 0.067.

The minimization in (4.2) allows the minimizers $u^{(i)}$ to differ by a constant across the interfaces Γ_i. This is the reason we employ the "soft" interface coupling as opposed to the $L^2(\Gamma_i)$-norm of $w^{(i+1,i)}$ which would enforce continuity across Γ_i. The boundary integral component of the total energy is a part of the $H^{1/2}(\Gamma_i)/\mathbb{R}$-norm. The form used in (4.2) does not include a negative power of $|x - y|$ as required by this fractional norm. Removal of the denominator allows large derivatives of $w^{(i+1,i)}$ to be present. At the same time, this term seems to be strong enough to keep both $u_h^{(i)}$, $u_h^{(i+1)}$ on order of h close to each other in $L^2(\Gamma_i)$-norm. The constraint (4.2b) controls the number of discontinuities in $\partial_y u$ across these interfaces. Hence the competition among the excess strain energy, the possible number of jumps in $\partial_y u$, and the soft coupling condition promote branching of the already established laminates across the interfaces Γ_i. The properties of the integral coupling term are demonstrated at Fig. 4 on a simple example.

This approach provides minimizers leading to lower energy levels corresponding to the second "multidimensional" scaling regime explained in the previous section. Another major benefit of the proposed approach is the computational cost. The method works well on coarse meshes—cf. Section 5—and it can be certainly implemented on parallel computers.

4.1. Domain Decomposition based on Equipartitioning of the Total Energy

In order to build a decomposition of Ω, i.e., to find the positions L_i of interfaces Γ_i, we face computationally almost impossible task of verifying the inequality (3.13) to find

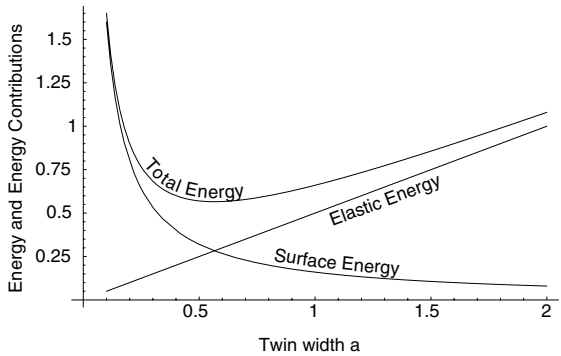

FIG. 5. Equipartitioning of the total stored energy $\alpha a + \epsilon \frac{L}{a}$ between the elastic part αa and the surface energy contribution $\epsilon \frac{L}{a}$. The two contributions intersect at the minimum of the total energy.

the dimension of the newly created space $V_h^{(i)}$. We use the equipartitioning of energy (Theorem 5 [15]) to get around this problem. The total energy is equipartitioned at equilibrium between energy of the elastic strain $\alpha \partial_x u$ and the surface energy (measured by the total variation $\epsilon \|\partial_{yy} u\|$); cf. Fig. 5. Namely, if u were a minimizer of the total energy (1.2) then

$$\epsilon \|\partial_{yy} u(x, .)\|(0, K) - \int_0^K \alpha \, |\partial_x u(x, y)|^2 \, dy = \kappa(\alpha, \beta, \epsilon, \Omega, u),$$
$$\text{for almost all } x \in (0, L). \quad (4.3)$$

It is possible to show [15] that the constant $\kappa(\alpha, \beta, \epsilon, \Omega, u)$ in (4.3) can be estimated, up to a multiplicative constant, by $\epsilon^{2/3} L^{-2/3}$. We cannot expect that (4.3) would be literally true in the finite dimensional setting. Rather, we assume that the equipartitioning holds true in an average sense with respect to the scale $(L_i - L_{i+1})$. Consequently, in view of (4.3), we construct the points $\{L_i\}_{i=1}^{M+1}$ by requiring

$$\int_{L_{i+1}}^{L_i} \epsilon \left\|\partial_{yy} u^{(i)}(x, .)\right\|(0, K) \, dx - \int_{L_{i+1}}^{L_i} \int_0^K \alpha \left|\partial_x u^{(i)}(x, y)\right|^2 \, dx \, dy$$
$$= C \left(\frac{\epsilon}{L}\right)^{2/3} (L_i - L_{i+1}) \quad (4.4)$$

for some positive constant C. We can simplify the search for the partitioning $\{L_i\}_{i=1}^{M+1}$ since we control the upper bound for the first integral in (4.4) by $\dim V_h^{(i)}$.

We determine the partitioning $\{L_i\}_{i=1}^{M+1}$ sequentially. Given Ω and $M > 1$ we first compute the initial iterate $u^{(1)}$ by solving the minimization problem

$$\mathcal{J}\left(u^{(1)}, \Omega\right) = \inf_{\substack{u \in W^{1,4}(\Omega) \\ u = 0 \text{ on } \partial\Omega \setminus \{x = L\} \\ \nabla u n = 0 \text{ on } \{x = L\}}} \mathcal{J}(u, \Omega),$$
$$\text{subject to } \int_0^L \epsilon \left\|\partial_{yy} u^{(1)}(x, .)\right\|(0, K) \, dx \le \epsilon^{2/3} L^{1/3} K. \quad (4.5)$$

Next, we set $\Omega_1 = \Omega$, $L_1 = L$, and we find the largest point L_2, $0 < L_2 < L_1$, such that

$$\int_{L_2}^{L_1}\int_0^K \alpha\left|\partial_x u_h^{(i)}(x,y)\right|^2 dx\,dy \sim C\left(\epsilon^{2/3}(L_1-L_2)^{1/3} - \left(\frac{\epsilon}{L}\right)^{2/3}(L_1-L_2)\right). \quad (4.6)$$

We continue by finding now two functions $u^{(1)}$, $u^{(2)}$ optimizing, in finite dimension and with $L_3 = 0$,

$$\min_{\substack{u^{(i)}\in V_h^{(i)}\\ i=1,2}} \sum_{i=1}^{2} \mathcal{J}\left(u_h^{(i)}, \Omega_i\right) + \gamma \int_{\Gamma_1}\int_{\Gamma_1} \left|w_h^{(2,1)}(x) - w_h^{(2,1)}(y)\right|^2 dx\,dy, \quad (4.7)$$

$$\text{where } w^{(2,1)} = u^{(2)} - u^{(1)}, \quad \gamma > 0, \quad \dim V_h^{(i)} \le \epsilon^{-1/3}(L_i - L_{i+1})^{-2/3}, \quad i = 1, 2.$$

We also require the following boundary conditions to be satisfied by the functions $u_h^{(i)}$ in the optimization (4.7)

$$\begin{aligned} u_h^{(2)}(x,y) &= 0, \quad \text{on } \partial\Omega_2\backslash\{\{x = L_2\}\cup\{x=0\}\},\\ u_h^{(1)}(x,y) &= 0, \quad \text{on } \partial\Omega_1\backslash\{\{x = L_2\}\cup\{x=L_1\}\},\\ \nabla u_h^{(1)}(x,y)n &= 0, \quad \text{on } \{x = L_1\}. \end{aligned} \quad (4.8)$$

Repeating this process, we split the domain $\Omega_2 = ((L_4, L_3)\cup(L_3, L_2))\times(0, K)$, $L_4 = 0$, so that (4.6) is satisfied with $i = 2$, and we then proceed to find three functions $u_h^{(i)}$ solving (4.7) but now with $i = 1, 2, 3$. We obtain a decomposition of domain Ω and we create a sequence of functions approaching the solution of Problem 4.1.

4.2. Computation of Descent Direction

We determine the solution to the minimization problem (4.2) by the Descent Algorithm. Let us denote

$$\begin{aligned} &\mathcal{E}\left(u^{(1)},\ldots,u^{(M)};\Omega_1,\ldots,\Omega_M\right)\\ &\quad\stackrel{\text{def}}{=} \sum_{i=1}^{M}\mathcal{J}\left(u^{(i)},\Omega_i\right) + \gamma\sum_{i=1}^{M-1}\int_{\Gamma_i}\int_{\Gamma_i}\left|w^{(i+1,i)}(x) - w^{(i+1,i)}(y)\right|^2 dx\,dy, \quad (4.9)\\ &\qquad\text{where } w^{(i+1,i)} = u^{(i+1)} - u^{(i)}, \quad \gamma > 0. \end{aligned}$$

Let $\mathbf{g} = (g^{(1)},\ldots,g^{(M)})$ be the metric gradient of $\mathcal{E}$ with respect to the $W^{1,4}(\Omega)$-topology. Letting $\mathbf{u} = (u^{(1)},\ldots,u^{(M)})$ with ith component corresponding to Ω_i, the update for the $(n+1)$-iterate of Steepest Descent is given by

$$\mathbf{u}_{n+1}^{(i)} = \mathbf{u}_n^{(i)} - \alpha_n \mathbf{g}_n^{(i)}, \quad \alpha_n \in \mathbb{R}^+. \quad (4.10)$$

The step length α_n is result of the line minimization

$$\alpha_n = \operatorname*{Arcmin}_{\alpha\in\mathbb{R}^+} \mathcal{E}(\mathbf{u} - \alpha\mathbf{g};\Omega_1,\ldots,\Omega_M). \quad (4.11)$$

In order to determine the descent direction $\mathbf{g}$ in the minimization problem (4.7) we proceed using the non-conforming domain decomposition method. We refer to [21] for its description. Denoting

$$d\mathcal{E}\big(\mathbf{u};\Omega_1,\dots,\Omega_M,\varphi^{(i)}\big) \stackrel{\text{def}}{=} \frac{d}{dt}\mathcal{E}\big(u^{(1)},\dots,u^{(i)}+t\varphi^{(i)},\dots,u^{(M)},\Omega_1,\dots,\Omega_j\big)\big|_{t=0},$$

the weak gradient $G(u^{(i)})|_{\Omega_i} \in W^{-1,4/3}(\Omega_i)$ be given by the variational relation

$$\big\langle G\big(u^{(i)}\big),\varphi^{(i)}\big\rangle_{W^{-1,4/3}(\Omega_i),W_0^{1,4}(\Omega_i)} = d\mathcal{E}\left(\mathbf{u};\Omega_1,\dots,\Omega_M,\varphi^{(i)}\right) \quad \text{for all } \varphi^{(i)} \in W_0^{1,4}(\Omega_i\backslash\Gamma_i). \tag{4.12}$$

Now, we find $g(u^{(i)})|_{\Omega_i} \in W_0^{1,4/3}(\Omega_i)$ by solving in the sense of distributions the following problem:

$$\begin{aligned} g\big(u^{(i)}\big) &= -\Delta^{-1}\,G\big(u^{(i)}\big), && \text{in } \Omega_i,\\ \nabla g\big(u^{(i)}\big)n &= \nabla g\big(u^{(i-1)}\big)n, && \text{for almost all } s\in\Gamma_i,\\ \int_{\Gamma_i}\big(g\big(u^{(i)}\big)(s)-g\big(u^{(i-1)}\big)(s)\big)\,\mu(s)\,dS &= 0, && \text{for all } \mu\in H^{1-14/24,24/14}(\Gamma_i),\\ g\big(u^{(i)}\big) &= 0 && \text{on } \partial\Omega. \end{aligned} \tag{4.13}$$

Denoting the unknown values $\nabla g(u^{(i)})n|_{\Gamma_i}$ by $\lambda^{(i)}$, i.e.,

$$\lambda^{(i)}(s) \stackrel{\text{def}}{=} \nabla g\big(u^{(i)}\big)n|_{\Gamma_i}(s), \quad \text{for almost all } s\in\Gamma_i, \tag{4.14}$$

the variational form of (4.13) reads: Find $g(u^{(i)}) \in W_0^{1,4/3}(\Omega_i\backslash\Gamma_i)$, and $\lambda^{(i)} \in H^{1/2}(\Gamma_i)$ such that

$$\begin{aligned} &\sum_{i=1}^{M}\int_{\Omega_i}\nabla g\big(u^{(i)}\big)(x)\nabla\varphi^{(i)}(x) - \sum_{i=1}^{M-1}\int_{\Gamma_i}\lambda^{(i)}(s)\big(\varphi^{(i)}(s)-\varphi^{(i-1)}(s)\big)\,dS\\ &\quad = d\mathcal{E}\big(\mathbf{u},\Omega_1,\dots,\Omega_M,\varphi^{(i)}\big), \quad \text{for all } \varphi^{(i)}\in W_0^{1,4}(\Omega_i\backslash\Gamma_i), \quad i=1,2,\dots,M, \quad \text{and}\\ &\int_{\Gamma_{i-1}}\big(g\big(u^{(i)}\big)(s)-g\big(u^{(i-1)}\big)(s)\big)\,\mu(s)\,dS = 0,\\ &\qquad\qquad \text{for all } \mu\in H^{1-14/24,24/14}(\Gamma_{i-1}), \quad i=2,\dots,M. \end{aligned} \tag{4.15}$$

Finally we project the descent direction into the space $W^{1,4}(\Omega)$ by taking

$$\left\{\nabla g\big(u^{(i)}\big)(x)\,\big\|\nabla g\big(u^{(i)}\big)(x)\big\|^{-2/3}\right\}_{i=1}^{M} \tag{4.16}$$

as the gradient of the new steepest (w. r. t. $W^{1,4}$-topology) descent direction $\mathbf{g}$.

4.3. Saddle Point Problem

The finite element discretization of the Saddle Point Problem (4.15) leads to the linear system

$$\begin{pmatrix} \mathbf{A} & \mathbf{B}^T \\ \mathbf{B} & \mathbf{0} \end{pmatrix} \begin{pmatrix} \mathbf{g}_h \\ \lambda_h \end{pmatrix} \begin{pmatrix} \mathbf{f} \\ \mathbf{0} \end{pmatrix} \tag{4.17}$$

where $\mathbf{A}$ is sparse, banded, block-diagonal, symmetric positive definite matrix given by

$$\mathbf{A} = \begin{pmatrix} \mathbf{A}_1 & \dots & \dots & \mathbf{0} \\ \mathbf{0} & \mathbf{A}_2 & \dots & \mathbf{0} \\ \dots & \dots & \dots & \dots \\ \mathbf{0} & \dots & \dots & \mathbf{A}_M \end{pmatrix}.$$

Each block diagonal matrix $\mathbf{A}_i$ corresponds to the stiffness matrix given by the discretization of the Laplace operator in the subdomain Ω_i. The matrix $\mathbf{B}$ is also a block matrix. It has the form

$$\mathbf{B} = (\mathbf{B}_1 \quad \dots \quad \dots \quad \mathbf{B}_M).$$

The square matrix $\mathbf{B}_i$ and (in general) the rectangular matrix $\mathbf{B}_{i-1}$ correspond to the discretization of the boundary integrals

$$\int_{\Gamma_{i-1}} \big(\varphi_l^{(i)}(s) - \phi_k^{(i-1)}(s)\big)\varphi_j^{(i)}\, dS = (\mathbf{B}_i)_{l,j} - (\mathbf{B}_{i-1})_{k,j}.$$

The test functions $\varphi^{(i)}$ are traces of the test functions used in the finite element space associated with the domain Ω_i while $\phi^{(i-1)}$ are traces of the test functions acting in the domain Ω_{i-1}.

We want to allow the increase of the number of discontinuities in $\partial_y u_h^{(i)}$ across the interfaces Γ_i. In view of the update (4.10) this means that the gradient descent directions $g_h^{(i)}$ must be discontinuous across these interfaces. This can only happen if

$$\mathbf{B}_i g_h^{(i)}\big|_{\Gamma_i} - \mathbf{B}_{i-1} g_h^{(i-1)}\big|_{\Gamma_i} = 0 \tag{4.18}$$

can be solved by two different vectors $g_h^{(j)}|_{\Gamma_j}$, $j = i, i-1$. Since $\mathcal{N}(\mathbf{B}_i) = \{0\}$, we must have two different matrices associated with each interface Γ_i. We use the same polynomial space in every subdomain Ω_i; thus we achieve this by using misaligned meshes; cf. Fig. 6. The origin of the new oscillations at the interfaces Γ_i is visible in Figs. 7 and 8.

Remark 4.4. The nonconforming domain decomposition itself will not promote formation of multidimensional structures. Approximating the optimization problem (4.2) with

$$\dim V_h^{(i)} = \dim V_h^{(i+1)}, \quad \text{for } i = 1, 2, \dots, M-1$$

and with meshes exactly aligned across the interfaces is equivalent in the Finite Element setting to finding a single function $u_h \in V_h \subset C^0(\Omega)$ minimizing the stored energy. The

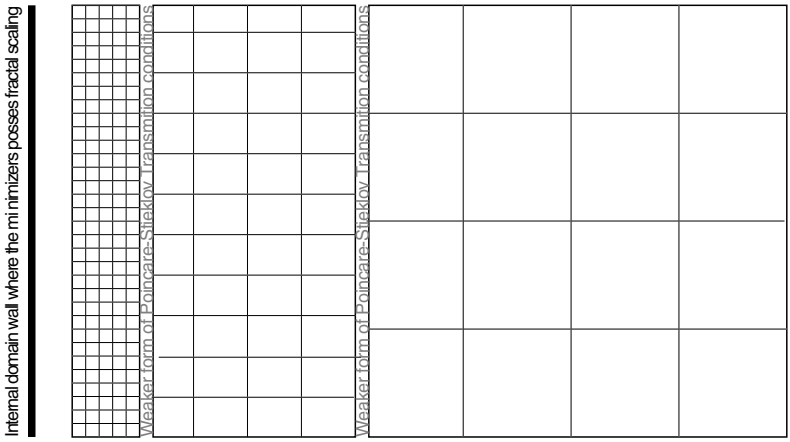

FIG. 6. Misaligned mesh used in the decomposition of Ω.

calculations performed in [13] show that the appearance of finer structures is due to larger-scale nonconformity which is promoted by the appearance of different matrices in (4.18). By how much the functions $u_h^{(i)}$ can differ across the interfaces Γ_i is controlled by the "soft" coupling boundary term in (4.2).

Remark 4.5. The implications of the mesoscale non-conforming approach are addressed in [13] in comparison with the conforming approximation of the self-similar minimizers.

5. NUMERICAL RESULTS

This section presents computational results obtained by the method introduced in the paper. We discuss the scaling properties corresponding to the minimizers obtained by this

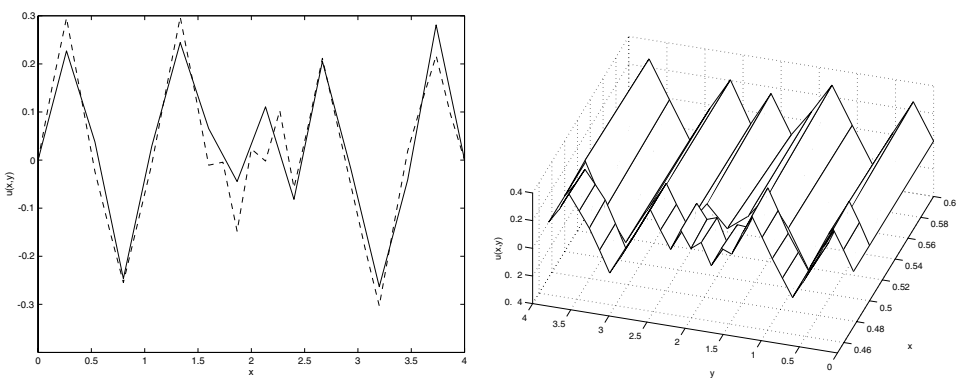

FIG. 7. Plots of minimizer u obtained from actual numerical calculations. We look at two functions at the interface Γ_1 located at $x = 1/2$. Left: This plot shows the profiles of functions $u^{(i)}(1/2, y),\ i = 1, 2$, for $y \in [0, 4]$. The dashed line corresponds to the function $u^{(2)}$ which belongs to the subdomain closer to $x = 0$. The solid line represents $u^{(1)}|_{\Gamma_1}$. We recall that the difference $u^{(1)} - u^{(2)}|_{\Gamma_1}$ is continuous in the sense (4.15b). Right: This figure shows the same functions along $x = 1/2$ but from a three dimensional perspective. The function with finer mesh corresponds to the dashed line on the left plot.

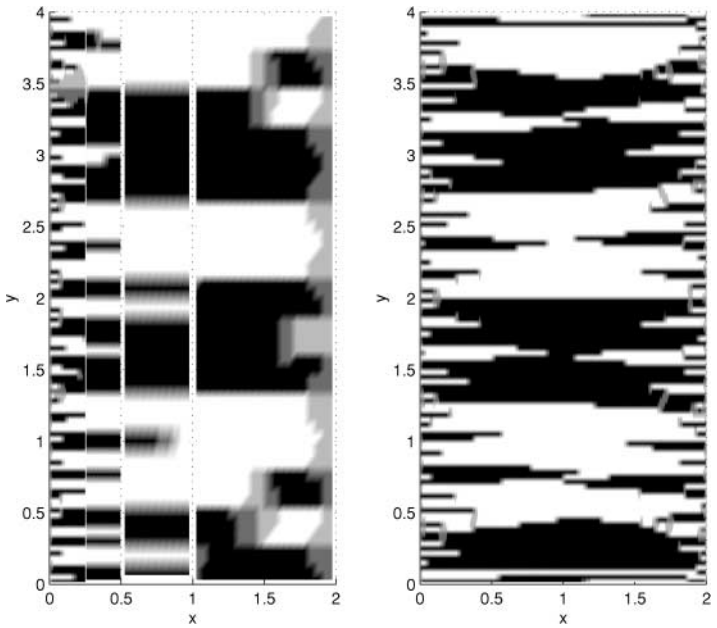

FIG. 8. The density plots of the deformation gradient for the calculations in "short" domains. The picture on the left corresponds to the calculations based on the methods introduced in the paper. The remaining picture corresponds to the standard globally continuous Q_1 Finite Element approximation.

method and we compare their scaling properties with the scaling properties of the minimizers based on the standard globally continuous Q_1 Finite Element approximation and on the functional (4.1), which does not contain contribution of the singular perturbation term.

We visualize the discrete minimizers using density plots based on the function

$$q(x, y) = \frac{\|\nabla u(x, y) - F_1\|}{\|\nabla u(x, y) - F_1\| + \|\nabla u - F_2\|} \in [0, 1] \tag{5.1}$$

where $F_1 = (0, 1)^T$ and $F_2 = (0, -1)^T$; F_1 and F_2 are the sought after gradients. The function $q(x, y)$ has values ranging from 0 to 1. If $\nabla u(x, y)$ is close to F_1 then $q(x, y)$ has value close to 0. Whereas, $q(x, y)$ is close to 1 if $\nabla u(x, y)$ is close to F_2. The colors prescribed to these values are black for 0 and white for 1.

All the results discussed in this section correspond to minimization of the problem (4.2). We take $\alpha = \frac{1}{2}, \beta = \frac{1}{4}$, and we set $\gamma = \frac{1}{2}, \epsilon = 0.04$. The decomposition of the computational domain we find is given by

$$(0, L) \times (0, 4) = \bigcup_{i=1}^{3} \left(\frac{L}{2^i}, \frac{L}{2^{i-1}} \right) \times (0, 4) \cup (0, 2) \times (0, 4)\,. \tag{5.2}$$

We choose the number of partitions in the x/y-directions to be 10/15, 20/30, 40/60, and 80/120 for $i = 1, 2, 3, 4$, respectively.The ratio of the dimensions of the Finite Element spaces corresponding to the domains with the common boundary is 0.25 in this case. The dimensions of the Finite Element spaces $V_h^{(i)}$ are 150, 600, 2400, and 9600, respectively. Thus the number of laminates near $\{x = 0\}$ can be, theoretically, 120 at the most. Using the local lower bound for the total number of discontinuities in the y-derivative of the

TABLE I
Equipartitioning of Energy and Number of Discontinuities

x_0	$\epsilon \int_0^{x_0} N_h(x)\,dx$	$\mathcal{J}(u_h(0,x_0)\times(0,4))$	Equipartitioning	$N_h(x_0)$	$[(9/4)^{1/3}\epsilon^{-1/3}x_0^{-2/3}4]$
1/16	0.11	0.18	−0.074	43	48
1/8	0.21	0.23	−0.028	39	30
1/4	0.38	0.32	0.052	35	19
1/2	0.65	0.48	0.155	27	12
1	1.03	0.76	0.240	19	7
2	1.47	1.19	0.221	11	5
3	1.75	1.48	0.182	7	4
4	1.87	1.65	0.103	3	4
5	1.91	1.80	−0.036	1	2
6	1.95	1.87	−0.095	1	2
7	1.99	1.87	−0.084	1	2
8	2.03	1.97	−0.173	1	1

Note. Summary of calculations verifying the equidistribution of energy (5.6) based on the value of the energy at various regions of the computational domain $\Omega = (0, 16) \times (0, 4)$. The discrete solution u_h is obtained by the nonconforming domain decomposition method. The "Equipartitioning" column contains the difference between the left-hand and right-hand sides of (5.6). The last column shows the predicted lower bound for the number of discontinuities. The lower bound is based on [17, Theorem 2.6]. We denote [.] the floor of a real number.

minimizers, we find that for the data used in our calculations

$$\|\partial_{yy}u(x_0,.)\|(0,4) \geq \frac{1}{2}C\,\frac{4}{\epsilon^{1/3}x_0^{2/3}}\bigg|_{C=(9/4)^{1/3},\epsilon=0.04,x_0=1/16} \sim 48. \tag{5.3}$$

Hence, the resolution in the y-direction in the subdomain $\Omega_4 = (0, 2) \times (0, 4)$, which is 120 is sufficiently large. The lower estimate (5.3) is based on the equipartitioning of the total energy and on the estimate of the constant C in (5.3) given by (Lemma 2.8 [17]). We note that in our calculations described in Section 5.1 the number of discontinuities at $x_0 = 1/16$ is 43; cf. Table I.

We assume throughout the analysis of the computational results that the constant in (4.3) is given by

$$\kappa(\alpha, \beta, \epsilon_h, (0, L) \times (0, 4), u_h) = \left(\frac{2\epsilon}{L}\right)^{\frac{2}{3}} \sim 0.03. \tag{5.4}$$

The results show that the minimizers obtained by the proposed method yield scaling $\alpha^{1/3}\epsilon^{2/3}L^{1/3}K$ of the total energy. We note that for the data used in our calculations

$$\sqrt{0.5 \times 0.04 \times 16} \times 4 \sim 2.26 > 0.93 \sim 0.5^{1/3} \times 0.04^{2/3} \times 16^{1/3} \times 4.$$

Hence, we should, as the first indication, observe energy roughly twice or three times smaller compared to the energy evaluated at the minimizers obtained by the standard globally continuous Q_1 Finite Element approximation. The later approach does not seem to provide the more complex pattern morphology.

5.1. Basic Comparison

We start the adaptive computational procedure with domain $\Omega_1 \stackrel{\text{def}}{=} (0, 16) \times (0, 4)$, discretized by 10 partitions along the x-direction and 15 partitions along the y-direction. This yields mesh size $h_1 = 1.600$ along the x-axis and the mesh size $h_2 = 0.2667$ along the y-axis. Subsequently, the domain is partitioned at $x = 8$. We keep the same mesh size and let $h_1 = h_1^{(1)} = 1.600$ and $h_2 = h_2^{(1)} = 0.2667$ in the subdomain $\Omega_1 = (8, 16) \times (0, 4)$. The new subdomain $\Omega_2 = (0, 8) \times (0, 4)$ has double the number of original partitions that we started with. This is the step in which we implicitly impose the constraint (4.2).

The subdomain $\Omega_2 = (0, 8) \times (0, 4)$ is split at the midpoint along the x-axis, i.e., at $x = 4$. We save the mesh size in the existing subdomains Ω_1 and Ω_2 and we double the number of partitions in the new subdomain $\Omega_3 = (0, 4) \times (0, 4)$. This yields 40 partitions along the x-axis and 60 partitions along the y-axis. The mesh size in the new subdomain is $h_1^{(2)} = 0.1000$ along the x-axis and $h_2^{(2)} = 0.0667$ along the y-axis.

Then the subdomain $\Omega_3 = (0, 4) \times (0, 4)$ is split again at the midpoint along the x-axis; in this case that is $x = 2$. Repeating the same procedure as before, we arrive at $h_1^{(4)} = 2/80 = 0.025$ and $h_2^{(4)} = 4/120 = 0.033$ for the subdomain $\Omega_4 = (0, 2) \times (0, 4)$.

In order to compare the calculations described above with the standard finite element method, we solve the same problem without the use of the decomposition and with the inclusion of the singular perturbation term. We take the regular grid of 640×120 points in the x- and y- directions, respectively, and we discretize the descent direction g corresponding to the functional (4.1) by Q_1-finite elements. We recall that $Q_1 = \text{Span}\{1, x, y, xy\}$. Thus we have a mesh size $h_1 = 0.025$ along the x-axis and a mesh size $h_2 = 0.03\overline{33}$ along the y-axis. This results in a system of 76, 800 linear equations for the descent direction g. The surface energy penalization is implicitly imposed by the fact that the minimizer cannot oscillate in the y-direction faster than $1/h_1$, i.e., $\xi_h(x) \leq 120$, for any $x \in (0, L)$. The resolution is identical in the region $(0, 2) \times (0, 4)$ for both calculations but we use only total of 12, 750 equations for the adaptive computational procedure.

The results from these calculations are plotted in Figs. 9, 10, and 11. Quick inspection of the first plot in Fig. 10 reveals the triangular domains characteristic for the simpler scaling regime in (2.2). The energies versus the iteration index n corresponding to the domain $(0, 1/2) \times (0, 4)$ are plotted at Fig. 12.

Remark 5.1. We do not include the "surface energy" term in our conforming calculations since we would have to use the squared laplacian of u as the representation of the surface energy. But then we would have to use a different finite element space than Q_1. Though it is possible to relate the two models on the continuum level it is problematic to do so on the discrete level. We simply assume that the role of the surface energy is played by the dimension of the approximating space. The discrete minimizer is thus determined by the competition between the different terms in (4.1) and this dimension based on the initial guess. Its footprint is always present in the final solution.

5.2. Computation of $\int_0^{x_0} N_h(x)\,dx$

We describe in this subsection the computation of the term $\int_0^{x_0} N_h(x)\,dx$ for $x_0 = 1/8$. The values of the integral for other values of x_0 are obtained similarly. The integral

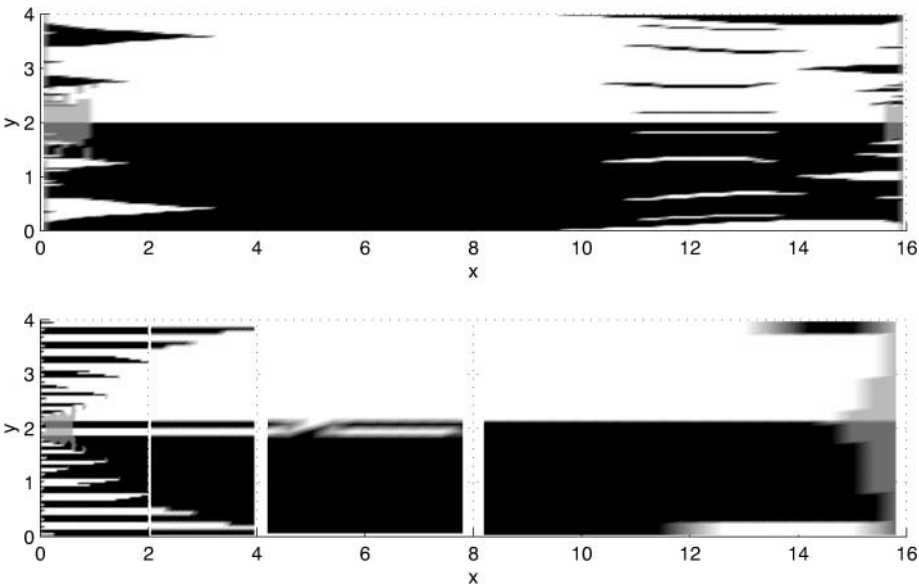

FIG. 9. Basic comparison of the results. The upper density plot corresponds to the minimization of (4.2) in the domain $(0, 16) \times (0, 4)$ discretized by the mesh 640×120 points in the x- and y-directions, respectively. The density plot exhibits characteristic "triangular regions" observed by Lifshitz [18]. The lower density plot visualizes the result of the minimization of the same problem but computed with the proposed method. This minimizer corresponds to the more complicated domain structure [20]. The spatial resolution in the region $(0, 2) \times (0, 4)$ is the same for both examples. The white stripes running across the lower density plot correspond to the positions of the interfaces Γ_i due to the use of the nonconforming domain decomposition.

$\int_0^{x_0} N_h(x)\,dx$ is the product of the number of discontinuities in $\partial_y u_h$ in the y-direction multiplied by the size of the interval $(0, x_0)$. Consequently, we approximate

$$\int_0^{1/8} N_h(x)\,dx \sim \frac{1}{16} N\left(\frac{1}{16}\right) + \left(\frac{1}{8} - \frac{1}{16}\right) N\left(\frac{1}{8}\right). \tag{5.5}$$

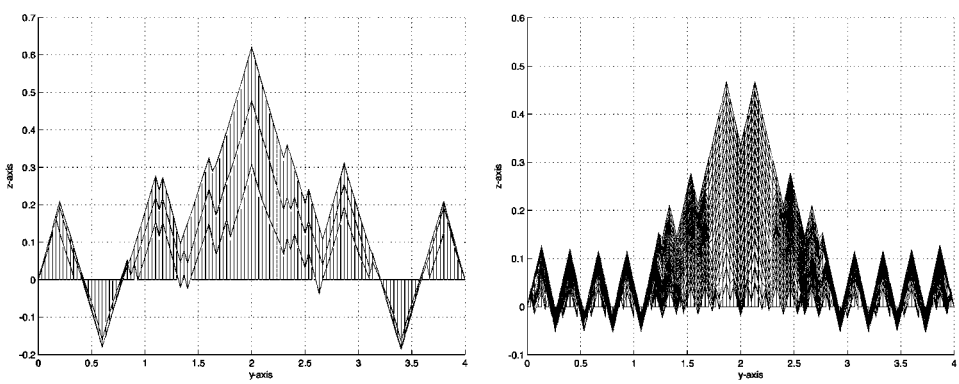

FIG. 10. Frontal views corresponding to the minimizers of (4.2) for the first example. The left plot corresponds to the minimization of (4.2) using the standard Q_1 finite element method. Comparison of the two plots reveals much finer oscillations contained in the minimizer found by the adaptive scaling approach. This is visible close to the boundary at $\{x = 0\}$. Number of oscillations on the right picture is 43 at $x = 1/16$, which almost exactly corresponds to the theoretical predictions.

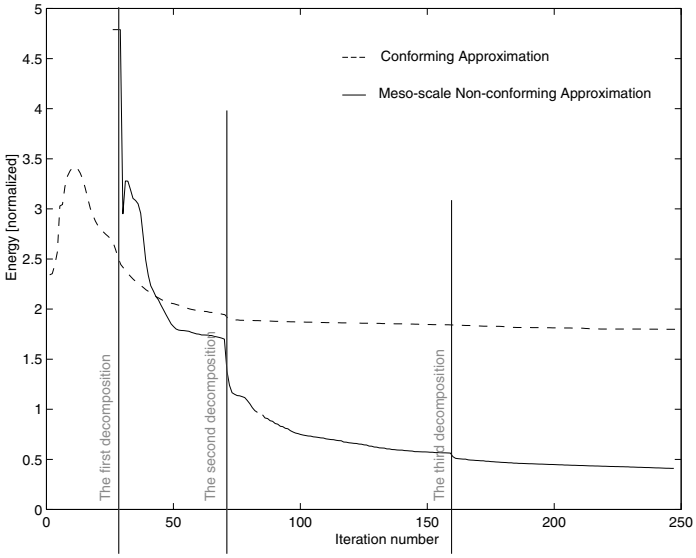

FIG. 11. Comparison of energies. The plot shows the value of $\mathcal{J}(u_h, (0, 1/2) \times (0, 4))$ against the Steepest Descent iteration number. The dashed line correspond to the minimization based on the standard Q_1 Finite Element approximation without any decomposition. The solid line represents the value of the energy for the minimizers obtained by the method introduced in the paper.

We read from Fig. 12 that

$$N\left(\frac{1}{16}\right) = 43 \quad \text{and} \quad N\left(\frac{1}{8}\right) = 39.$$

Thus

$$\int_0^{1/8} N_h(x)\,dx \sim \frac{43}{16} + \frac{39}{16} = \frac{41}{8} \approx 5.12.$$

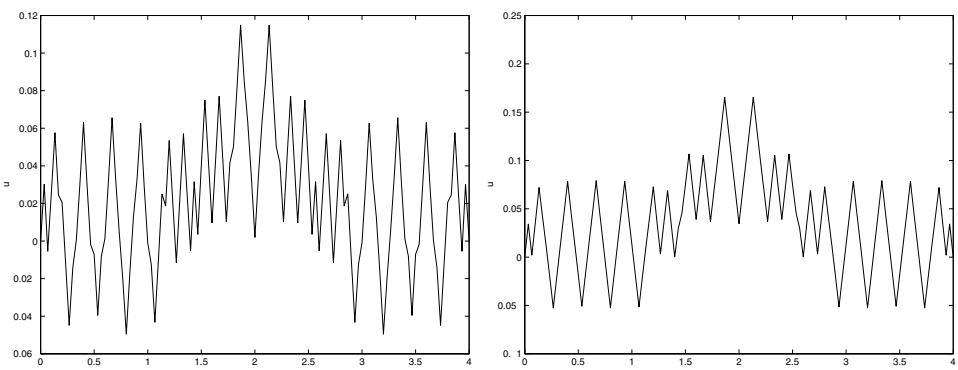

FIG. 12. Left: Plot of the function $u(x, y)$ at the point $x_0 = 1/16$. Right: Plot of the function $u(x, y)$ at the point $x_0 = 1/8$. The determination of the integral $\int_0^{1/8} N_h(x)\,dx$ uses the information provided by these figures. The integral is split into two integrals $\int_0^{1/16} N_h(x)\,dx$ and $\int_{1/8}^{1/16} N_h(x)\,dx$ which are computed separately. The term $N_h(x)$ corresponds number of discontinuities in $\partial_y u_h$ along y-direction. In the case of the left figure, we count 43 discontinuities. We multiply this by the length of subinterval $[0, 1/16]$ resulting in the value of $43/16$ for the first integral. The second integral is computed similarly with resulting value of $39/16$. Thus $\int_0^{1/8} N_h(x)\,dx \approx 41/8$.

5.3. Local Scaling Law

Now we proceed to identify a scaling law obtained by the method introduced in the paper. Recalling (4.3), it should be true that

$$\epsilon_h \int_0^{x_0} N_h(x)\,dx - \mathcal{J}(u_h, (0, x_0) \times (0, 4)) \approx x_0 \left(\frac{2\epsilon}{L}\right)^{\frac{2}{3}}, \quad 0 < x_0 \leq \frac{L}{2}. \tag{5.6}$$

The requirement $x_0 \leq \frac{L}{2}$ eliminates the influence of the boundary condition at $\{x = L\}$ where the energy is not zero. In other words, we do not assume that (5.6) holds in the "far field" in our calculations.

Table I summarizes verification of the formula (5.6) evaluated for $x_0 = 1/16, 1/8, 1/4$, and $x_0 = 1/2$ and at farther points in $[1, 8] \times [0, 4]$ as well as it indicates number of discontinuities created in the y-derivative of u_h. The solution u_h used in the table is obtained using the adaptive nonconforming domain decomposition method and the computational domain is $\Omega = (0, 16) \times (0, 4)$.

The last two columns compare computed and predicted number of discontinuities in the y-derivative of minimizers. The theory developed in [17, Theorem 2.6] provides a lower bound but it does not yield an upper bound for $N(x)$. Comparing the last two columns in Table I it is evident that $N_h(x)$ follows the same pattern as $\epsilon^{-1/3} x_0^{-2/3} K$. Hence the computational evidence confirms the conjecture made in [17] that there exists a constant C such that for the minimizers of (1.2) the following upper bound holds

$$\|\partial_{yy} u(x_0, .)\|(0, K)\,dy \leq C \epsilon^{-1/3} x_0^{-2/3} K. \tag{5.7}$$

Complex minimizers are expected to yield energy values that scale for $x_0 \ll L$ in the same way as the surface energy contribution. Namely,[4]

$$\mathcal{J}(u_h, (0, x_0) \times (0, K)) \propto \epsilon^{2/3} x_0^{1/3} K. \tag{5.8}$$

We summarize computed and predicted values of energy at Table 13 where we compare the "$\frac{2}{3}$" scaling with the "$\frac{1}{2}$" scaling law. The values of the energy used in this table are the same as those used in Table I.

5.4. Global Scaling Law Obtained with the Adaptive Domain Decomposition Method

We now focus on determining the scaling law best approximating the total stored energy values obtained for the results in domains $\Omega = (0, L) \times (0, 4)$, $L = 1, 2, 4, 8, 16$. Our objective is to find constants C_1 and C_2 such that

$$\epsilon \int_0^{L/2} N_h(x)\,dx + \mathcal{J}(u_h, (0, L/2) \times (0, 4)) \sim \begin{cases} C_1 \sqrt{\alpha \epsilon_h \frac{L}{2}}, & \text{or} \\ C_2\, \alpha^{1/3} \epsilon_h^{2/3} \left(\frac{L}{2}\right)^{1/3}, \end{cases}$$
$$\text{for } L = 1, 2, 4, 8, 16. \tag{5.9}$$

The surface energy term $\epsilon \int_0^{L/2} N_h(x)\,dx$ is not present in our calculations explicitly. We control the interplay between the surface energy and the stored elastic energy by the domain

[4] An anonymous referee brought to our attention results in [6] proving the cited hypothesis.

decomposition which obeys the equipartitioning principle (4.4), and by the dimension of the approximating space which has the upper bound (3.12) derived from the scaling law of the surface energy. Hence, we can legitimately expect the scaling behavior (5.9).

First, we compute the values of the scaling laws (5.9) for each of the domains $(0, L) \times (0, 4)$, $L = 1, 2, 4, 8, 16$. Then, we solve for the corresponding constants C_1 and C_2. We divide the computed energy by the anticipated scaling law, i.e.,

$$\begin{aligned} C_{1,L} &= \frac{\epsilon \int_0^{L/2} N_h(x)\,dx + \mathcal{J}(u_{h,L}, (0, L/2) \times (0, 4))}{\sqrt{\alpha \epsilon L/2}} \\ C_{2,L} &= \frac{\epsilon \int_0^{L/2} N_h(x)\,dx + \mathcal{J}(u_h, (0, L/2) \times (0, 4))}{\alpha^{1/3} \epsilon^{2/3} (L/2)^{1/3}} \end{aligned} \tag{5.10}$$

These computations are shown in Table II. We identify a scaling law by the *Mean deviation* of the constants. We choose the scaling law based on the smallest range of fluctuations of the "constants" in (5.10). The calculations presented suggest that

$$\begin{aligned} &\int_0^{L/2} \epsilon N_h(x)\,dx + \mathcal{J}(u_h, (0, L/2) \times (0, 4)) \\ &\quad \sim \begin{cases} 1.1 \times \sqrt{0.5 \times 0.04 \times L/2} \times 4, & \text{if } L \le 4, \\ 4.2 \times 0.5^{1/3} \times 0.04^{2/3} \times (L/2)^{1/3} \times 4, & \text{if } L \ge 4. \end{cases} \end{aligned} \tag{5.11}$$

This observation is based on the results summarized in Table III. Thus it seems that the "$\frac{1}{2}$" scaling law provides better predictions if $L \le K$ and the "$\frac{2}{3}$" scaling law is better if $L \ge K$.

An interesting observation is to note that for the case $[0, 4] \times [0, 4]$, both scaling laws in (5.11) yield almost identical value of energy. The case $L = 4$ achieves a sort of optimality or it is a critical point "of sorts".

5.5. Local-in-*y* Scaling Law Conjecture

In this section we analyze the local-in-y scaling law conjecture made in [17]. Namely, the question is if there exists a constant C, independent of ϵ, such that

$$\int_{Q_l} |\partial_x u_h|^2 \, dx\, dy + \int_0^l \epsilon \|\partial_{yy} u_h(x, .)\| \left(0, l^{2/3}\right) dx \le C\, \epsilon^{2/3} l, \tag{5.12}$$

TABLE II
Local Scaling Law

x_0	$\mathcal{J}(u_h(0, x_0) \times (0, 4))$	$\epsilon^{2/3} x_0^{1/3} 4$	$\epsilon^{1/2} x_0^{1/2} 4$
1/16	0.18	0.18	0.20
1/8	0.23	0.23	0.28
1/4	0.32	0.29	0.4
1/2	0.48	0.37	0.56
1	0.76	0.46	0.80
2	1.19	0.58	1.13

Note. Summary of summarizes calculations verifying the local scaling properties of the minimizers obtained using the method introduced in the paper.

TABLE III
Values of Constants $C_{1,L}$ and $C_{2,L}$

$L/2$	$\epsilon \int_0^{L/2} N_h(x)\,dx + \mathcal{J}(u_{h,L}, (0, L/2) \times (0, 4))$	$C_{1,L}$	$C_{2,L}$
1/2	$0.2 + 0.38$	**1.02**	1.56
1	$0.4 + 0.55$	**1.18**	2.03
2	$1.25 + 1.2$	2.16	**4.15**
4	$1.55 + 1.64$	1.99	**4.29**
8	$2.03 + 1.97$	1.77	**4.27**
Variance		*0.24*	*1.82*
Median deviation		*0.39*	*0.13*

Note. These values are computed as described by (5.10). The first column corresponds to the domain range along x-axis. The second column is the total stored energy in the corresponding domain, i.e., in $(0, L/2) \times (0, 4)$. The function u_h is obtained by the method introduced in the paper.

where $Q_l = [0, l] \times [a, a + l^{2/3}]$. The conjecture is based on the self-similar construction which provides the upper estimate $C\epsilon^{2/3}L^{1/3}$ for the energy (1.2). We note that certain minimizers are indeed asymptotically self-similar [6], which makes this conjecture realistic. We find that this conjecture, at least for the calculations presented here, is indeed true. The value of the constant seems to be 2. We present Table IV associated with the calculations done on $\Omega = (0, 16) \times (0, 4)$ using the method introduced in the paper and described in Section 5.1. We take $a = 0$ for the purpose of verification of (5.12).

5.6. Analysis of the Minimizers Obtained with the Globally Continuous Q_1 Finite Element Approximation

We now attempt to identify a scaling law associated with the standard approach, that is, one that does not involve the decomposition of the domain $\Omega \stackrel{\text{def}}{=} (0, 16) \times (0, 4)$ and which

TABLE IV
Local-in-y Scaling Law Conjecture

l	$\int_{Q_l} \lvert\partial_x u_h\rvert^2\,dx\,dy + \int_0^l 0.04 \lVert\partial_{yy} u_h(x, .)\rVert(0, l^{2/3})\,dx$	$2 \times 0.04^{\frac{2}{3}} l$
1/40	0.003	0.005
3/80	0.005	0.008
1/16	0.010	0.014
1/10	0.018	0.023
1/8	0.023	0.029
1/4	0.059	0.058
3/10	0.063	0.070
1/2	0.117	0.116
3/4	0.225	0.175
4/5	0.239	0.187

Note. This table shows the sum of local and surface energies in region $Q_l = [0, l] \times [0, l^{2/3}]$ and the conjectured power law $\epsilon^{2/3} l$; [17]. The value of the surface energy coefficient in our calculations is taken to be $\epsilon = 0.04$. The function u_h is obtained by the method introduced in the paper. The corresponding calculation is described in Section 5.1.

TABLE V

$\epsilon_h \int_0^{x_0} N_h(x)\,dx - \mathcal{J}(u_h, (0, x_0) \times (0, 4)) = x_0(\frac{\epsilon_h}{8})^{\frac{2}{3}}$

x_0	$\int_0^{x_0} N_h(x)\,dx$	$\mathcal{J}(u_h, (0, x_0) \times (0, 4))$	ϵ_h
1/16	1.56	0.38	0.25
1/8	3.12	0.65	0.21
1/4	5.5	0.90	0.17
1/2	7.75	1.28	0.17
1	12.25	1.82	0.15
2	17.25	2.45	0.15
3	22.25	2.74	0.13
4	23.25	2.81	0.13
5	24.25	2.81	0.13
6	25.25	2.81	0.13
7	25.25	2.81	0.12
8	27.25	2.81	0.12

Note. Summary of calculations of the "surface energy" coefficient ϵ_h. This table contains energy values calculated using the discrete solution obtained by standard finite element method. We use the regular grid of 640×120 points in the x- and y-directions, and we discretize the descent direction g corresponding to the functional (4.1) by Q_1-finite elements, $Q_1 = \text{Span}\{1, x, y, xy\}$. The mesh size is $h_1 = 0.025$ along the x-axis and $h_2 = 0.0\overline{33}$ along the y-axis. This results in a system of 76, 800 linear equations for the descent direction g.

is based only on the minimization of the functional defined by (4.1). Since the surface energy term is not included directly in this computation, we determine the "surface energy" coefficient using the equidistribution of energy. Hence, we assume that this principle holds true even without the explicit inclusion of the penalization term. We present in Table V the values of ϵ_h corresponding to each $x_0 = 1/16, 1/8, 1/4, 1/2, 1, 2, 3, \ldots, 8$. The values of the coefficient ϵ_h oscillate around 0.15 for $x_0 \geq 1/4$. Similar calculations done for $L = 1 - 8$ seem to be more consistent in terms of the value of the "surface energy" coefficient ϵ_h. The results are presented in Table VI including the constants $C_{i,L}$, $L = 1 - 16$, $i = 1, 2$.

The computation of $\int_0^{x_0} N_h(x)\,dx$, found in the second column of Table V, is described in Section 5.2. So we refer the reader to this section for verification as we proceed to describe and discuss the computation of constants $C_{1,L}$ and $C_{2,L}$. As before, we compute the two anticipated scaling laws using (5.9) with ϵ_h obtained from the standard Q_1 Finite Element approximations. We then use these scaling laws to compute the constants via the relationship given by (5.10). Table VI contains the computed values of these constants. We note that all the scaling laws yield a median deviation far above the ones for the constants in Table III. However, an inspection of the energy plots in Fig. 13 indicates that the standard Q_1 Finite Element approximation yields lower values of energy for the "short" domains, $L \leq 4$. This observation is corroborated by the fact that the values of the "surface energy" coefficient ϵ_h obtained from the standard Q_1 Finite Element calculations are smaller for $L = 1, 2$ than 0.04, which is the value of the surface energy coefficient we use implicitly in the method introduced in the paper. We conclude that the standard Q_1 Finite Element method approximates the first scaling regime, $\sqrt{\alpha\epsilon L}$, for $L \leq 4$, better than the method we introduce.

TABLE VI
Values of Constants $C_{1,L}$ and $C_{2,L}$

$L/2$	$\epsilon_{h,L}$	$\mathcal{J}(u_{h,L}, (0, L/2) \times (0, 4))$	$C_{1,L}$	$C_{2,L}$
1/2	0.02	0.11	1.56	2.37
1	0.03	0.44	3.59	5.74
2	0.03	0.72	4.16	7.46
4	0.06	1.51	4.36	7.82
8	0.15	2.81	3.63	4.68
Variance			*1.24*	*4.68*
Median deviation			*0.53*	*1.19*

Note. The first column corresponds to the domain range along the x-axis. The third column is the total stored energy in the corresponding domain. The table corresponds to the standard Q_1 Finite Element approximations. Since the median deviation of the values in the $C_{1,L}$ column is twice smaller compared to the same quantity for the $C_{2,L}$ column, we conclude that the these calculations approximate the "$\frac{1}{2}$"-power law.

5.7. Branching of the Needle Twin Structures

One of the characteristic properties of the minimizers corresponding to lower values of the energy is that their derivatives, or gradients, oscillate with higher and higher frequency closer to the internal crystal surfaces. This corresponds to splitting the already stable structures. We observe this phenomenon by visually comparing the density plots for four calculations with $K = 1, 2, 4$, and 16 in the domain $(0, 16) \times (0, K)$. Comparing the results we notice that while there is only one generation of splitting of the twin lamella for $K = 1$, there are four generations of splitting visible for $K = 16$. We also point out that our minimizers look somewhat different from what is suggested in Section 1 and the theory developed in [15–17]. The twin structure is not subdivided into just one or two smaller twins but away from the boundary $\{x = 0\}$ it splits many times.

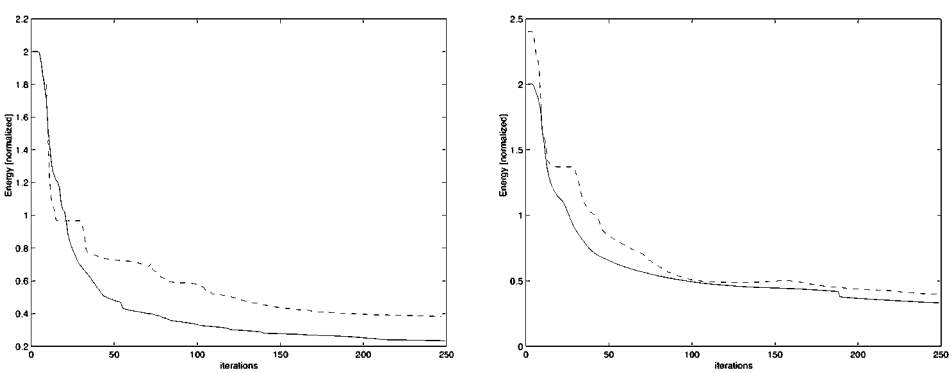

FIG. 13. The plots of the energy $\mathcal{J}(u_h, (0, 1/8) \times (0, 4))$. The plot on the left corresponds to the domain $\Omega = (0, 1) \times (0, 4)$; the plot on the right is based on the calculations in $\Omega = (0, 2) \times (0, 4)$. The two plots confirm the observation that the standard Q_1 Finite Element approximation adheres to the coarser "$\frac{1}{2}$"-scaling law which is preferable for "short" domains. In these cases it outperforms the method introduced in the paper. On the other hand the Q_1 Finite Element approximation does not provide any conclusive scaling behavior for "long" domains when a multiscale behavior of the pattern morphology is to be expected. The dashed line corresponds to the energy computed using the method introduced in the paper.

TABLE VII
Measured and Predicted Twin Widths

x_0	Measured width	Prediction $0.04^{1/3}x_0^{2/3}$
1/16	0.16-0.2	0.13
1/8	0.16-0.2	0.17
1/4	0.16-0.2	0.21
1/2	0.25-0.4	0.27
1	0.25-0.66	0.34
2	0.25-1.5	0.43
3	0.25-1.75	0.49
4	2	0.54

Note. We assume that the twin width is proportional to $\epsilon^{1/3}x_0^{2/3}$ where x_0 is the distance to the internal surface at $x = 0$. The measurements correspond to the function u_h obtained by the method introduced in the paper, and to calculations described in Section 5.1.

The width of the twins changes due to the splitting. The scaling law (3.11) and the equidistribution principle (4.3) imply that

$$\text{averaged twin width at distance } x_0 \text{ from } \{x = 0\} \propto \epsilon^{1/3}x_0^{2/3}. \tag{5.13}$$

Table VII summarizes the width scaling observed in our calculations.

REFERENCES

1. G. Alberti and S. Müller, A new approach to variational problems with multiple scales, *Comm. Pure Appl. Math.* **LIV** (2001), 697–715.
2. J. M. Ball and R. D. James, Proposed experimental tests of a theory of fine microstructure and the two wells problem, *Phil. Trans. Rogal Soc. London* **338A** (1991), 389–450.
3. F. S. Bates and G. H. Fredrickson, Block copolymers: Designer soft materials, *Phys. Today* **52-2** (February 1999), 32–38.
4. R. Choksi, Scaling laws in microphase separation of dibloc copolymers, *J. Nonlin. Sci.* **11** (2001), 223–236.
5. R. Choksi and R. Kohn, Bounds on the micromagnetic energy of a uniaxial ferromagnet, *Comm. Pure. Appl. Math.* **LI** (1998), 259–289.
6. S. Conti, Branched microstructures: scaling and asymptotic self-similarity, preprint: Max-Planck Institute (1999), no. 73, to appear in *Comm. in Pure and Appl. Math.*
7. S. Conti, I. Fonseca, and G. Leoni, A γ-convergence result for the two-gradient theory of phase transitions, *Comm. in Pure and Appl. Math.* **LV** (2002), 857–936.
8. B. Dacorogna and P. Marcellini, *Implicit Partial Differential Equations* (Birkhäuser, 2000).
9. C. J. Garcia-Cervera and E. Weinan, Effective dynamics for ferromagnetic thin film, submitted (2001).
10. T. Y. Hou, P. Rosakis, and P. LeFloch, A level-set approach to the computation of twinning and phase-transitions dynamics, *J. Comput. Phys.* **150** (1999), 302–331.
11. P. Klouček, Remarks on compactness in the formation of fine structures, in *Applied Nonlinear Analysis*, edited by A. Sequeira, Advanced Mathematics Programme (Pitman, 1998).
12. P. Klouček and M. Luskin, Computational modeling of the martensitic transformation with surface energy, *Math. Comput. Modelling* **20**(10/11) (1994).
13. P. Klouček and Luis A. Melara, The computational modelling of internal surfaces in crystals, Technical Report: École Polytechnique Fédérale de Lausanne, Département de Mathématiques, Analyse et Analyse Numérique (August, 2001), no. 12.

14. P. Klouček and Luis A. Melara, The computational modelling of micromagnetic fine structures in uniaxial ferromagnets using nonconforming domain decomposition method, ENUMATH 2001, European conference on Numerical Mathematics and Advanced Applications, July 23–28, 2001, Ischia Porto, Italy (January, 2002).
15. R. Kohn and S. Müller, Branching of twins near an austenite-twinned-martensite interface, *Philos. Magazine* **66A** (1992), 697–715.
16. R. Kohn and S. Müller, Relaxation and regularization of nonconvex variational problems, *Rend. Sem. Mat. Fis. Univ. Milano* **62** (1992), 89–113.
17. R. Kohn and S. Müller, Surface energy and microstructure in coherent phase transformations, *Comm. Pure Appl. Math.* **47** (1994), 405–435.
18. E. Lifshitz, On the magnetic structure of iron, *J. Phys.* **VIII** (1944), no. 6, 337–346.
19. Y. Nishuira and I. Ohnishi, Some mathematical aspects of the micro-phase separation in diabloc copolymers, *Physica D* **84** (1995), 31–39.
20. I. A. Privorotskij, *Thermodynamic Theory of Domain Structures* (Wiley, New York, 1976).
21. A. Quarteroni and A. Valli, Domain Decomposition Methods for Partial Differential Equations (Oxford University Press, Oxford, 1999).
22. E. K. H. Salje, Phase Transitions in Ferroelastic and Co-elastic Crystals: An Introduction for Mineralogist, Material Scientists and Physicist, the student ed., vol. 1 (Cambridge, University Press, 1993).
23. P. J. Swart and P. J. Holmes, Energy minimization and the formation of microstructure in dynamic anti-plane shear, *Arch. Rat. Mech. Anal.* **121** (1992), 37–85.
24. W. P. Ziemer, *Weakly Differentiable Functions*, Graduate Texts in Math. (Springer-Verlag, New York, 1989).